

# Sparse Gaussian Process Potentials: Application to Lithium Diffusivity in Superionic Conducting Solid Electrolytes

Amir Hajibabaei, Chang Woo Myung, and Kwang S. Kim\*

*Center for Superfunctional Materials, Department of Chemistry and Department of Physics,  
Ulsan National Institute of Science and Technology, Ulsan 44919, Korea*

(Dated: May 21, 2021)

For machine learning of interatomic potentials a scalable sparse Gaussian process regression formalism is introduced with a data-efficient on-the-fly adaptive sampling algorithm. With this approach, the computational cost is effectively reduced to those of the Bayesian linear regression methods whilst maintaining the appealing characteristics of the exact Gaussian process regression. As a showcase, experimental melting and glass-crystallization temperatures are reproduced for  $\text{Li}_7\text{P}_3\text{S}_{11}$ , Li diffusivity is simulated, and an uncharted phase is revealed with much lower Li diffusivity which should be circumvented.

## I. INTRODUCTION

A solid with ionic conductivity similar to liquid electrolytes has far reaching implications for the energy storage industry. Recently, first-principles (FP) calculations have been applied extensively for theoretical studies of ionic diffusion in solid electrolytes [1]. But due to the huge computational resources required for the electronic structure calculations these simulations are often applied only to small systems ( $\sim 100$  atoms) and short intervals of time ( $\sim 100$  ps). Moreover, due to the Arrhenius-type temperature dependence of the diffusion events in solids, they occur too slowly at room temperature to be sampled with statistical certainty using ab initio molecular dynamics (AIMD) [2]. Therefore often simulations are carried out at elevated temperatures and ionic diffusivity at room temperature is approximated by extrapolation.

As an alternative to FP calculations, it has been demonstrated that machine learning (ML) methods can be applied for accurate representations of the potential energy surface (PES). Most notably, neural-network (NN) representations [3], Gaussian approximation potentials (GAP) [4], gradient-domain [5] and symmetrized gradient-domain ML [6], deep potential [7], compressed sensing [8], and deep neural-network for molecular wavefunctions [9] are among various ML techniques which have been implemented. Using these techniques, the PES is learned from the data (potential energy and forces) obtained from limited FP calculations. For generation of the relevant data, on-the-fly learning [10–13], a query-by-committee active-learning [14], and global exploration of PES [15] have been reported.

Training of neural-networks scale linearly with the size of data  $n$  but they contain a huge number of optimizable parameters and require big data to avoid over-fitting. On the other hand, the kernel methods where a covariance matrix is constructed and inverted, are (almost) non-parametric but scale as  $n^2$  for construction and  $n^3$  for inversion of the covariance matrix. Considering that a

single FP calculation for a system with  $N$  atoms yields  $3N + 1$  data components (energy and forces), the size of covariance matrix becomes huge even with a small number of training data. Because of this unfavorable scaling, a critical issue is balancing of the global exploration versus local exploitation in sampling the data. For instance, in some on-the-fly learning algorithms the ML model is continuously updated during MD which keeps the model locally accurate but undermines its transferability.

Here we explore low-rank approximations of the covariance matrix and sparse Gaussian process regression (SGPR) [16, 17] for improving the scalability and an adaptive sampling algorithm for optimal on-the-fly generation of the training data and global exploration. We study the lithium diffusivity in solid electrolytes to explore possible superionic conducting materials towards fast charging inflammable batteries.

## II. SPARSE GAUSSIAN PROCESS REGRESSION POTENTIALS

Assuming that the force on atom  $i$  in a chemical system depends only on the relative coordinates of atoms  $j$  in its neighborhood, the local chemical environment (LCE) of  $i$  is defined as

$$\rho_i = \{\vec{r}_{ij}; j \neq i \ \& \ |\vec{r}_{ij}| < r_c\} \quad (1)$$

where  $r_c$  is the cutoff for neighborhood relations. The optimal cutoff can be obtained by balancing the errors of the regression algorithm and the random noise caused by ignoring the atoms beyond the cutoff [18]. Since any configuration  $x$  of  $N$  atoms is compiled to a list of LCEs  $x = \{\rho_i\}_{i=1}^N$ , the potential energy becomes additive over local terms

$$E(x) = \sum_{i=1}^N \varepsilon(\rho_i) \quad (2)$$

where  $\varepsilon$  is a fictional latent function. The common theme for all Bayesian regression methods is defining a covariance kernel  $\mathcal{K}(\rho_i, \rho_{i'})$  which encodes the similarity

\* kimks@unist.ac.kr

of LCEs and is invariant with respect to the symmetry operations that leave the potential energy invariant e.g. translations and rotations [19]. It models the covariance between local energies:  $\mathcal{K}(\rho_i, \rho_{i'}) \propto \langle \varepsilon(\rho_i) \varepsilon(\rho_{i'}) \rangle$ . We assume that the kernel is normalized:  $0 \leq \mathcal{K}(\rho_i, \rho_{i'}) \leq 1$ . The kernel for a pair of configurations  $(x, x')$  becomes

$$\mathcal{K}(x, x') = \sum_{i \in x, i' \in x'} \mathcal{K}(\rho_i, \rho_{i'}). \quad (3)$$

The training data consists of a set of configurations  $X = \{x_j\}_{j=1}^n$  as inputs along with their potential energies and forces obtained from FP calculations as targets  $Y$ . For brevity, in the following we only consider potential energies  $Y = \{E_j\}_{j=1}^n$ . By representing  $\varepsilon$  as a Gaussian process it is assumed that the targets are sampled from a distribution given by [16]

$$Y|X \sim \mathcal{N}(0, \beta(k_{nn} + \sigma^2\mathbb{I})) \quad (4)$$

where  $k_{nn}$  is the covariance matrix  $\mathcal{K}(x_i, x_j)$  amongst the data,  $\mathcal{N}$  is a multivariate Gaussian distribution,  $\beta$  is the scale of variance and  $\sigma$  the scale of random noise in  $Y$ .  $\sigma, \beta$  and other hyper-parameters which may be defined in  $\mathcal{K}$  are optimized by maximizing the log-likelihood of  $Y$ . For a test configuration  $x^*$ , the predictive distribution  $E^*$  for the potential energy becomes

$$E^*|x^*, X, Y \sim \mathcal{N}(\mathcal{E}, \Sigma) \quad (5)$$

$$\mathcal{E} = k_{*n}(k_{nn} + \sigma^2\mathbb{I})^{-1}Y \quad (6)$$

$$\Sigma = \beta(k_{**} - k_{*n}(k_{nn} + \sigma^2\mathbb{I})^{-1}k_{*n}^\top) \quad (7)$$

where  $k_{*n}$  is the covariance matrix for  $x^*$  and data  $X$ ,  $\mathcal{E}$  is the predictive mean, and  $\Sigma$  is the predictive variance. Eq. 6 is the defining equation for Gaussian process regression (GPR). This calculation requires inversion of a large covariance matrix which scales as  $\mathcal{O}(n^3)$ .

For improving the scalability, one can exploit the LCE similarities in the data  $X$ . It is very likely that many LCE pairs in  $X$  are similar:  $\mathcal{K}(\rho, \rho') \approx 1$ . Let  $z = \{\chi_j\}_{j=1}^m$  denote a reduced set of LCEs which are significantly distinct from each other and are sufficient statistics for  $X$ .  $z$  is called the inducing set of LCEs. The key for a SGPR model is low-rank approximation of the covariance matrices [16]

$$\begin{aligned} k_{nn} &\approx k_{nm}k_{mm}^{-1}k_{nm}^\top \\ k_{*n} &\approx k_{*m}k_{mm}^{-1}k_{nm}^\top \end{aligned} \quad (8)$$

where  $k_{mm}$  is the covariance matrix amongst  $z$ ,  $k_{nm}$  cross covariance between  $X$  and  $z$ , and  $k_{*m}$  between  $x^*$  and  $z$ . Using the Woodbury matrix identity, this results in a predictive mean given by

$$\begin{aligned} \mathcal{E} &\approx k_{*m}\mu \\ \mu &= (\sigma^2k_{mm} + k_{nm}^\top k_{nm})^{-1}k_{nm}^\top Y. \end{aligned} \quad (9)$$

It is worth noting that if  $k_{mm}$  in the above expression is replaced by  $\gamma^{-2}\mathbb{I}$ , this formalism will be reduced to the

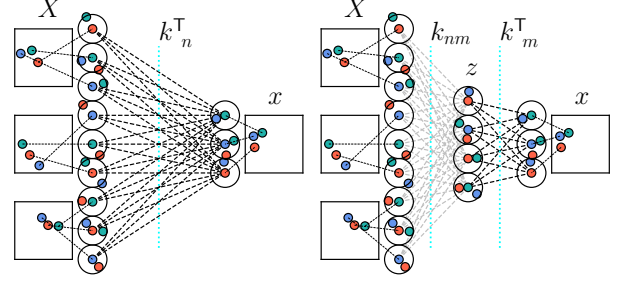


FIG. 1. Schematic comparison of GPR (left) and SGPR (right). Squares represent atomic configurations. Circles represent compilation of configurations into LCEs around each atom. In GPR the potential energy for  $x^*$  is predicted by calculating its covariance matrix with the data  $X$ . In SGPR only the covariance matrix with the inducing LCEs  $z$  is needed.

Bayesian linear regression (BLR) method [12]. In linear regression algorithms [8, 12], regardless of a regularization term, the linear system  $k_{nm}\mu = Y$  is solved while  $\mu$  in Eq. 10 is the solution of

$$\begin{bmatrix} k_{nm} \\ \sigma L^\top \end{bmatrix} \mu = \begin{bmatrix} Y \\ \mathbf{0} \end{bmatrix} \quad (11)$$

where  $L$  is the Cholesky factor of  $K_{mm}$  and  $\mathbf{0}$  is a column vector of zeros with length  $m$ . Therefore converting BLR to SGPR is straightforward. On the other hand, normal GPR is recovered if we set  $z = X$ . Also note that if we substitute  $\mu = k_{mm}^{-1}w$  in Eq. 9 it looks like a GPR based on  $(z, w)$  on behalf of  $(X, Y)$ . Therefore this approximation is also called projected process (PP). SGPR and PP are distinguished only in defining the loss function for optimizing the hyper-parameters and selection of  $z$ . In SGPR the variational lower-bound of the true log marginal likelihood introduced by Titsias [17] should be maximized. Inclusion of the forces data in regression is formulated in the Supplemental Material (SM) [20]. A useful quantity that indicates the covariance loss due to sparsification is

$$s(\rho) = k(\rho, \rho) - k_{\rho m}k_{mm}^{-1}k_{\rho m}^\top \quad (12)$$

which is referred to as the spilling factor [21] but it is also proportional to the predictive variance of a GPR based on  $(z, w)$ .

After projection, only  $z$  and  $\mu$  are needed for predictions, reducing the computational cost to  $\mathcal{O}(m)$  instead of  $\mathcal{O}(nN)$  (see Fig. 1). For calculating  $\mu$  we only need to invert a matrix of size  $m$  which is much smaller than  $(3N + 1)n$  as in full GPR. The total cost for calculation of  $\mu$  is proportional to  $(3N + 1)nm^2 \ll (3N + 1)^3n^3$  [22]. Considering that the kernel itself is usually computationally expensive, the cost of constructing the related covariance matrices is even more important. Since in SGPR we only need to calculate the kernel between the data and inducing LCEs, a significant improvement is achieved in comparison with full GPR. In a naive comparison the improvement is  $\mathcal{O}(n^2) \rightarrow \mathcal{O}(n)$ , but a more

rigorous analyses in SM shows a much better improvement. For example with 100 configuration (100 atoms each), the improvement is a factor of  $\mathcal{O}(10^3)$ .

### III. THE KERNEL

For a similarity kernel between LCEs, the smooth overlap of atomic positions (SOAP) is defined as [19]

$$\mathcal{K}(\rho_i, \rho_{i'}) = \int d\mathbf{R} \left| \int d\vec{r} \xi_i(\vec{r}) \xi_{i'}(\mathbf{R}\vec{r}) \right|^2 \quad (13)$$

where  $\mathbf{R}$  is the 3D rotations operator,  $\xi_i(\vec{r})$  is the atomic density in neighborhood of  $i$

$$\xi_i(\vec{r}) = \sum_{j \in \rho_i} e^{-\alpha |\vec{r} - \vec{r}_{ij}|^2}, \quad (14)$$

and  $\alpha$  is a hyper-parameter. Analytical integration results in [19]

$$\mathcal{K}(\rho_i, \rho_{i'}) \propto \sum_{l, m, m'} \frac{1}{2l+1} (I_{mm'}^l)^* I_{mm'}^l \quad (15)$$

where

$$I_{mm'}^l = \sum_{\substack{j \in \rho_i \\ j' \in \rho_{i'}}} e^{-\alpha(r_j^2 + r_{j'}^2)/2} \iota_l(\alpha r_j r_{j'}) Y_l^m(\hat{n}_j) (Y_l^{m'}(\hat{n}_{j'}))^*, \quad (16)$$

$r_j = |\vec{r}_{ij}|$ ,  $\hat{n}_j = \vec{r}_{ij}/r_j$ , and  $\iota_l$  is the modified Bessel function of the first kind (Bessel-i).  $\iota_l$  can be expanded as [23]

$$\iota_l(\alpha r_j r_{j'}) = \sum_{n=0}^{\infty} a_{nl} r_j^{2n+l} r_{j'}^{2n+l} \quad (17)$$

where  $a_{nl} = (\alpha/2)^{2n+l}/(n+l)!n!$ . Here, we use this expansion to simplify the kernel into an inner product

$$c_{nlm}^i = \sqrt{a_{nl}} \sum_{j \in \rho_i} \Theta(r_j) e^{-\alpha r_j^2/2} r_j^{2n+l} Y_l^m(\hat{n}_j) \quad (18)$$

$$I_{mm'}^l = \sum_n c_{nlm}^i (c_{nlm'}^i)^* \quad (19)$$

$$p_{nn'l}^i = \sum_m \frac{c_{nlm}^i (c_{n'l m}^i)^*}{\sqrt{2l+1}} \quad (20)$$

$$\mathcal{K}(\rho_i, \rho_{i'}) \propto \sum_{n, n', l} p_{nn'l}^i (p_{nn'l}^{i'})^* \quad (21)$$

$\Theta$  in Eq. 18 is a smooth cutoff function which is manually inserted for elimination of discontinuities in the kernel and its gradients upon atoms entering to/exiting from the LCEs. The  $a_{nl}$  multipliers decrease extremely fast by increasing  $n$  and  $l$ ; therefore it suffices to calculate up to only a few orders of expansion. In our calculations  $\alpha = 1$ ,  $r_c = 8$ ,  $\Theta(r) = (1 - r/r_c)^2$ , and  $l, n \leq 3$ .

Extension to multi-species environments is straightforward. Species-dependent LCE becomes  $\rho_i = \{\rho_i^\alpha\}$  where  $\alpha$  indexes the species present in  $\rho_i$ . Then the coefficients in Eq. 18 are calculated separately for each atomic species ( $c_{nlm}^i \rightarrow c_{nlm}^{i\alpha}$ ) and the total descriptor vector becomes [24]

$$p_{nn'l}^{i\alpha\beta} = \frac{1}{\sqrt{2l+1}} \sum_m c_{nlm}^{i\alpha} (c_{n'l m}^{i\beta})^* \quad (22)$$

The generalized multi-species kernel becomes [24]

$$\mathcal{K}(\rho_i, \rho_{i'}) = \mu_{s_i s_{i'}} \left( \sum_{\substack{\alpha, \alpha', \beta, \beta', \\ n, n', l}} p_{nn'l}^{i\alpha\beta} (p_{nn'l}^{i'\alpha'\beta'})^* \nu_{\alpha\alpha'} \nu_{\beta\beta'} \right)^\eta \quad (23)$$

where  $\nu_{\alpha\beta}$  is an alchemical similarity kernel between the atomic species in LCEs and  $\mu_{s_i s_{i'}}$  is a kernel which depends on the species of the atoms  $i, i'$  and quantifies the covariance between local energies. Here we have chosen  $\nu_{\alpha\beta} = \delta_{\alpha\beta}$  and  $\mu_{s_i s_{i'}} = \delta_{s_i s_{i'}}$ . The latter corresponds to summation of independent Gaussian processes defined for each atomic species. The exponent  $\eta$  controls the sensitivity of the kernel which is fixed at 4 in this work. As usual, the kernel is normalized by

$$\mathcal{K}(\rho_i, \rho_{i'}) \rightarrow \frac{\mathcal{K}(\rho_i, \rho_{i'})}{\sqrt{\mathcal{K}(\rho_i, \rho_i) \mathcal{K}(\rho_{i'}, \rho_{i'})}} \quad (24)$$

### IV. ON-THE-FLY SAMPLING

The most important step, regardless of the regression algorithm, is generation of the data. Early methods [3, 4] prepared the data beforehand which is not efficient. On-the-fly learning methods [10–13] estimate the accuracy of the potential and use a criterion for data generation. In GPR based algorithms the predictive variance is a suitable criterion while in NNs the uncertainty can be emulated by training identical NNs with different initial random seeds. Generally, GPR based algorithms are more suited for on-the-fly learning since they have only a few hyper-parameters. But the size of these potentials and their computational cost grow with time, therefore the data generated earlier need to be dumped to keep the potential affordable. Thus for globally accurate potentials, it is critical to devise an optimal adaptive sampling algorithm. We tackle this issue by replacing the predictive variance by another criterion which we call the geometric criterion. This is motivated from the observation that the predictive variance does not take advantage of energy and forces data. Briefly, aside from hyper-parameter optimization, a SGPR potential can be modified in two ways: adding a LCE  $\chi$  to the inducing set  $z$ , adding a snapshot  $x$  to the data  $X$ . Instead of calculating the predictive variance, we calculate the change in the predictive mean of the potential by directly constructing the

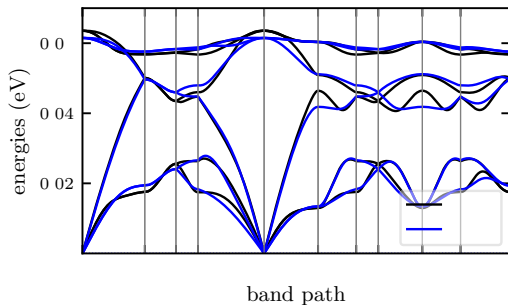


FIG. 2. Phonon spectra of bulk Si with a SGPR potential generated using only 13 DFT data and 36 inducing LCEs.

potential both with and without  $x$  (same for  $\chi$ ). If the change in the predictive mean is more than a threshold  $\epsilon$  the addition is accepted (See SM [20] for algorithm).

## V. COMPUTATIONAL DETAILS

The VASP [25] package which implements the projector augmented-wave [26] approach to DFT with PBE GGA functionals [27] is used for all FP calculations. Calculations are non-spin-polarized and kinetic energy cutoff of 500 eV is applied. We have developed the python package AutoForce for generating SGPR models and on-the-fly learning of the PES [28]. This package is coupled with the atomic simulation environment (ASE) [29] and from there it can be coupled to various FP software including VASP. Phonon spectra for Si is calculated using the phonopy [30] package.

MD with a ML potential is referred to as MLMD. For reporting the accuracy of ML potentials, we use root mean squared error (RMSE) and coefficient of determination which is denoted as  $R^2$  in statistics and is defined by

$$R^2 = 1 - \frac{\sum_i (f_i - \tilde{f}_i)^2}{\sum_i (f_i - \bar{f})^2} \quad (25)$$

where  $\{f_i\}$  are FP forces,  $\bar{f}$  is their average, and  $\{\tilde{f}_i\}$  are ML forces.  $R^2$  indicates the fraction of explained variance.

## VI. SILICON

For a benchmark simulation, we created a SGPR potential for bulk Si since it has been studied by several other ML methods [3, 4, 10, 11, 13]. A cubic cell with 64 atoms was chosen with a  $2 \times 2 \times 2$  k-point grid for DFT calculations. The potential is generated by on-the-fly sampling with MD simulations at 300 K (for 20 ps) and 1000 K (for 30 ps). Using the algorithm ULTRAFast

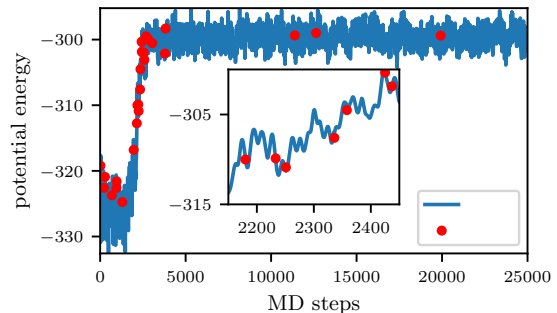


FIG. 3. On-the-fly MLMD with the adaptive sampling algorithm for Si at 2000 K. The time-step for MD is 2 fs. Melting occurs at steps  $\sim 2000$  to  $\sim 3000$ . The system is liquid beyond that.

(see SM), only 13 DFT calculation are performed for data generation and 36 LCEs are sampled as the inducing set. This entire simulation took less than 1 h. 100 snapshots are chosen from trajectories for testing which result in the RMSE=0.07 eV/Å and  $R^2 = 0.994$  for forces. Additionally we tested the model by calculating the phonon spectra with a  $5 \times 5 \times 5$  supercell which is shown in Fig. 2. Direct comparison with previous methods is not possible since they model Si with different levels of generality. A similar study is on-the-fly active learning [13] which reached the RMSE of 0.08 eV/Å with 133 DFT calculations for 10 ps MD at 620 K. It is worth noting that this simulation based on normal GPR, using only two body and three body descriptors, took 64 h. Thus our SGPR algorithm is more than  $\sim 300$  times faster despite using the much more expensive SOAP descriptor and smaller computational resources (20 cores instead of 32).

RMSE of ML potentials usually increase with temperature because of larger forces and more disorder. In Si simulation above from 300 to 700 K RMSE increases from 0.03 to 0.07 eV/Å. However, at higher temperatures larger RMSE can be tolerated because of random forces due to thermal fluctuations. In Ref [3] a silicon melt simulation with NN errors well above 0.2 eV/Å accurately reproduced the DFT radial distribution function. A minimal requirement is that distribution of forces error should be Gaussian centered at 0. As such, they act as random forces due to thermal coupling with a heat bath and do not significantly alter the thermodynamics.

In order to show the performance of the algorithm in disordered phases, we continued the simulation for Si at 1500 and 2000 K, each for 50 ps. At 1500 K, the model did not change much (only 2 additional DFT calculations). But at 2000 K, the system melted which caused dozens of new DFT calculations. After the melting completed, the model had learned the liquid phase and only a few DFT calculations were invoked in the remaining steps (see Fig. 3). At the end, the model had accumulated 42 DFT data and 141 inducing LCEs, and RMSE

was  $\sim 0.15 \text{ eV}/\text{\AA}$  at 2000 K. In conclusion, the SGPR algorithm can learn the disordered phases with a small number of DFT calculations as well.

## VII. SULPHIDE SOLID ELECTROLYTES

For an example of solid electrolytes, a SGPR model is generated by training in  $\text{Li}_3\text{PS}_4$  ( $\alpha$  and  $\beta$  phases) and  $\text{Li}_7\text{P}_3\text{S}_{11}$  crystals. During total of  $\mathcal{O}(10^5)$  MD steps, only 111 FP data and 705 inducing LCEs are sampled. To verify the model with data independent from training, we performed lengthy MLMD simulations for  $\text{Li}_7\text{P}_3\text{S}_{11}$  at several temperatures in the range 300 to 700 K and  $10^3$  snapshots are randomly selected from trajectories. For this testing set,  $\text{RMSE}=0.14 \text{ eV}/\text{\AA}$  and  $R^2 = 0.944$ . Training and testing are discussed in more details in SM [20]. The SGPR potential is perfectly stable, as demonstrated by the energy conservation test (see SM), and during MD it never reached a non-physical arrangement of atoms which is a common worry for ML potentials.

We used this model for large scale MLMD simulations of  $\text{Li}_7\text{P}_3\text{S}_{11}$  ( $4 \times 2 \times 2$  supercell, 672 atoms) in isothermal-isobaric (NPT) ensemble at several temperatures in the range 300 to 1200 K and external pressure of  $10^5 \text{ Pa}$ . For this size, our implementation of MLMD is  $\mathcal{O}(10^4)$  faster than AIMD. The mean squared displacement (MSD) of atoms, defined by

$$\text{MSD}(t) = \frac{1}{N} \sum_{i=1}^N |\Delta \vec{r}_i(t)|^2 \quad (26)$$

where  $N$  is the number of mobile ions and  $\Delta \vec{r}_i(t) = \vec{r}_i(t) - \vec{r}_i(0)$ , is shown in SM. A phase transition is detected by MLMD (at  $T \geq 450$ ) which occurs by rotations of the  $\text{P}_2\text{S}_7$  double-tetrahedra into a new orientational order. In the following, the initial and the new structures are referred to as  $\alpha$  and  $\beta$  phases. The ground state energies of  $\alpha$  and  $\beta$  phases obtained from exact DFT calculations (VASP/PBE) are  $-4.413$  and  $-4.416 \text{ eV}$  per atom respectively which shows that they are almost isoenergetic and that  $\beta$  phase is not an artifact of the SGPR potential. Also, examples from  $\beta$  phase are encountered during training and testing.  $0.14 \text{ eV}/\text{\AA}$  is the lumped RMSE for both phases. In Fig. 4 the mean absolute error (MAE) of ML is shown in the vicinity of  $\alpha \rightarrow \beta$  transition. The two steps in the MSD of S atoms correspond to delayed rotations of  $\text{P}_2\text{S}_7$  double-tetrahedra in different layers. The delay is  $\sim 0.5 \text{ ns}$  at 450 K with a  $4 \times 2 \times 2$  supercell (see Fig. S7 in SM). The  $\alpha$ - and  $\beta$ - $\text{Li}_7\text{P}_3\text{S}_{11}$  crystal structure information files, visualizations, and radial distribution functions (RDFs) are available as SM. The  $\alpha \rightarrow \beta$  transition is captured in a movie. Specifically in the range 450 to 600 K the system remains a few hundred ps in the  $\alpha$ -phase before transition to the  $\beta$ -phase which allows us to estimate the Li diffusivity in both phases. In agreement with experimental reports [31, 32], at 900 K,

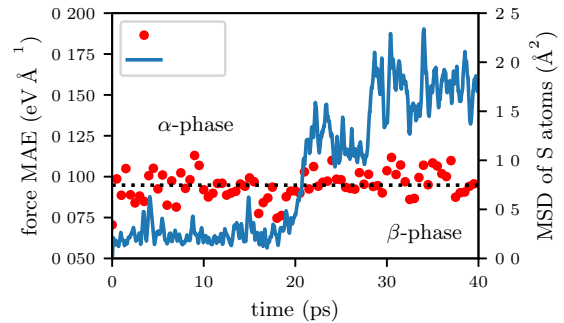


FIG. 4. MAE of MLMD in the vicinity of  $\alpha \rightarrow \beta$  phase transition in  $\text{Li}_7\text{P}_3\text{S}_{11}$  at 500 K ( $2 \times 1 \times 1$  supercell). Since the transition occurs by rotation of S atoms in  $\text{P}_2\text{S}_7$  double-tetrahedra, MSD of S atoms is a direct indicator.

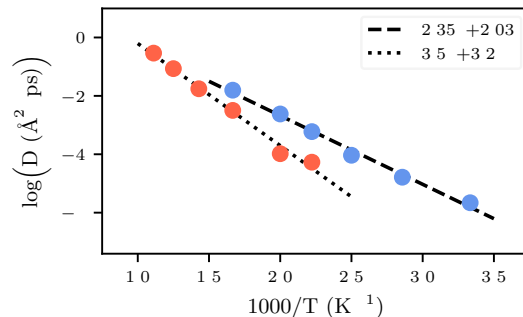


FIG. 5. Li diffusivity ( $D$ ) in  $\alpha$  (blue) and  $\beta$  (red) phases of  $\text{Li}_7\text{P}_3\text{S}_{11}$ .

the P and S atoms also start to diffuse, which indicates melting or its decomposition to more stable components (see SM for RDF).

The diffusion coefficient (diffusivity) is defined as

$$D = \lim_{t \rightarrow \infty} \frac{1}{2dt} \langle \text{MSD}(t) \rangle \quad (27)$$

where  $d = 3$  is dimensions and  $\langle \rangle$  indicates the ensemble average (see Fig. 5). With the assumption of an Arrhenius temperature dependence for diffusivity

$$D = D_0 e^{-E_a/k_B T}, \quad (28)$$

we calculate the activation energies  $E_a$  of 0.20 eV and 0.30 eV in  $\alpha$  and  $\beta$  phases, respectively. The Nernst-Einstein relationship for conductivity  $\sigma$  is given by

$$\sigma = \frac{Nq^2}{Vk_B T} D \quad (29)$$

where  $N$  is number of Li atoms,  $V$  is volume,  $q$  is ions electric charge, and  $T$  is temperature. The ionic conductivity in  $\alpha$  phase at RT(=300 K) becomes

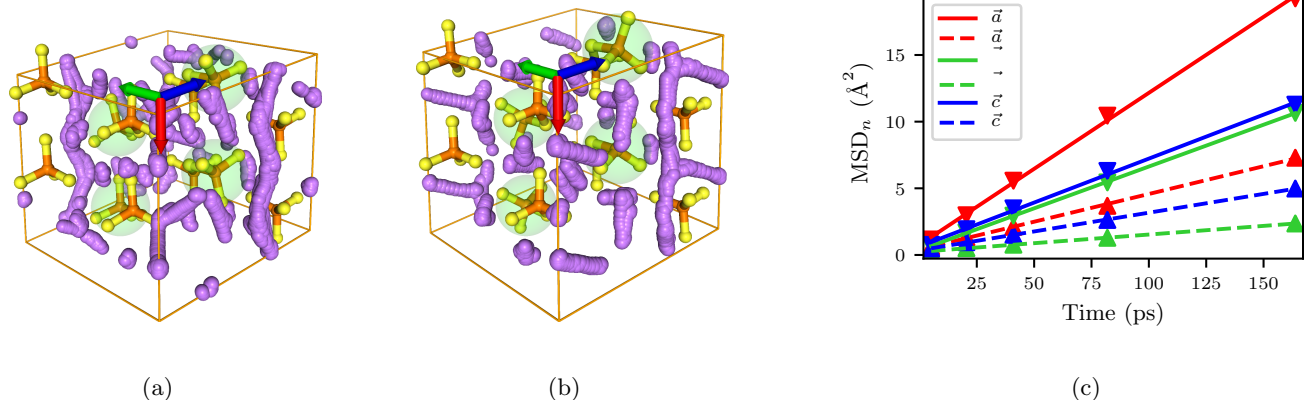


FIG. 6. Time-lapse of the Li positions over a few hundred ps in (a)  $\alpha$  and (b)  $\beta$  phases of  $\text{Li}_7\text{P}_3\text{S}_{11}$  with a  $2 \times 1 \times 1$  cell at 300 K. (c) Directional MSD in  $\alpha$  and  $\beta$  phases sampled by MD with a  $4 \times 2 \times 2$  cell at 450 K. The respective unit cell vectors ( $\vec{a}$ ,  $\vec{b}$ ,  $\vec{c}$ ) are indicated with red, green and blue vectors in (a) and (b).

$3.5 \times 10^{-2}$  S/cm from direct simulation at this temperature which is in reasonable agreement with previous reports of  $5.7 \times 10^{-2}$  [33] and  $4.5 \times 10^{-2}$  S/cm [34]. For  $\beta$  phase, the RT conductivity is obtained by extrapolation of  $D$  and approximating  $V$  (which is  $T$ -dependent) by the volume of the relaxed cell. This yields the conductivity of  $2.3 \times 10^{-3}$  S/cm which is more than an order of magnitude lower than  $\alpha$  phase. Alternatively one can assume Arrhenius dependence for  $\sigma T$  and extrapolate. The numerical difference is  $\mathcal{O}(1\%)$  since the volume of  $\alpha$  phase expands less than 1% (300 to 600 K) and  $\beta$  phase about  $\sim 4\%$  (450 to 800 K).

Diffusion pathways are visualized in Fig. 6. In  $\alpha$  phase, the diffusion of Li atoms is highly concerted. By re-orientation of some of  $\text{PS}_4$  tetrahedra in  $\beta$  phase, this concerted diffusion is somewhat scattered. For a more quantitative explanation, the directional MSD along  $\hat{n}$  is defined by

$$\text{MSD}_{\hat{n}}(t) = \frac{1}{N} \sum_{i=1}^N |\Delta \vec{r}_i(t) \cdot \hat{n}|^2. \quad (30)$$

As shown in Fig. 6c, the diffusivity is the largest along the  $\vec{a}$ -axis in both phases. The main difference is that the diffusivity along  $\vec{b}$  and  $\vec{c}$  axes are almost equal in  $\alpha$  phase, while in  $\beta$  phase this symmetry is clearly broken. In Ref [33], it is pointed out that the one-dimensional MSD of Li atoms along one of the axes in  $\text{Li}_7\text{P}_3\text{S}_{11}$  is nearly a factor of 2 higher than that along the other two axes. This is consistent with the directional MSD that we report for  $\alpha$ - $\text{Li}_7\text{P}_3\text{S}_{11}$  in Fig. 6c. They also suggest that the Li ionic motion is highly collective in agreement with our simulations. The concerted motion of Li atoms in  $\alpha$  phase is also demonstrated in the supplemented movie.

The glass  $\text{Li}_7\text{P}_3\text{S}_{11}$  is created by a melt-quench simulation from 1200 to 300 K. The Li conductivity of  $9.3 \times 10^{-3}$  S/cm is then obtained for the glass phase (with MLMD for 3 ns) which is higher than the conduc-

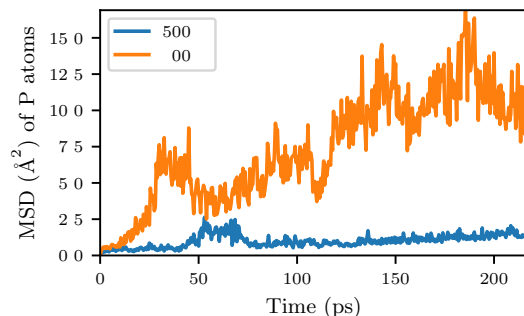


FIG. 7. MSD of P atoms in glass phase  $\text{Li}_7\text{P}_3\text{S}_{11}$ . Diffusion of these atoms at 600 K allows the glass to slowly relax and eventually crystallize.

tivity in  $\beta$  phase. Equilibration of the glass at higher temperatures (Fig. 7) shows that P atoms start to diffuse at 600 K which indicates crystallization, in agreement with experiment [31, 32, 35]. In liquid and glass phases RMSE=0.21 eV/ $\text{\AA}$  and  $R^2 = 0.917$  (see SM).

Experimentally,  $\text{Li}_7\text{P}_3\text{S}_{11}$  is often prepared in glass-ceramic phase by controlled crystallization and heat treatment of the glass phase. Depending on the heat treatment conditions, ionic conductivities of  $3.2 \times 10^{-3}$  and  $1.7 \times 10^{-2}$  S/cm are reported [32, 35]. It was shown that the experimental conductivity is correlated with the degree of crystallisation, depending on the heat treatment method [36]. Experimental measurements of the ionic conductivity with techniques such as impedance spectroscopy probe the long-range dynamics of Li which is influenced by the properties such as grain boundaries, degree of amorphism, etc. Wohlmuth et al. [37] probed the short-range diffusivity of Li in glass-ceramic  $\text{Li}_7\text{P}_3\text{S}_{11}$  and showed that the activation energy of bulk  $\text{Li}_7\text{P}_3\text{S}_{11}$  is 0.20 eV, in agreement with our simulation.

### VIII. CONCLUSION

In conclusion, we used the SGPR formalism for generating accurate, stable, and scalable interatomic potentials which, in the cases of  $\text{Li}_7\text{P}_3\text{S}_{11}$ , described the Li diffusivity and melting/crystallization (from glass phase) temperatures, consistent with experiment. An uncharged crystal structure is found for this material which is nearly iso-energetic to the known crystal structure but has a much lower Li diffusivity. This phase should be avoided for better Li conductivity. The SGPR algorithm is obtained by low-rank approximation of the covariance

matrix in exact GPR and offers a much better scalability. The computational cost of SGPR scales roughly similar to the Bayesian linear regression methods. We also showed that converting BLR to SGPR is straightforward and can be beneficial specially for active/on-the-fly machine learning of interatomic potentials.

This work was supported by NRF (National Honor Scientist Program: 2010-0020414), UNIST (A.I. Incubation Project Fund: 1.210091.01), and KISTI (KSSC-2018-CHA-0057, KSC-2019-CRE-0253, KSC-2020-CRE-0146).

- 
- [1] Z. Deng, Y. Mo, and S. P. Ong, Computational studies of solid-state alkali conduction in rechargeable alkali-ion batteries (2016).
- [2] X. He, Y. Zhu, A. Epstein, and Y. Mo, Statistical variances of diffusional properties from ab initio molecular dynamics simulations, *npj Computational Materials* **4**, 18 (2018).
- [3] J. Behler and M. Parrinello, Generalized Neural-Network Representation of High-Dimensional Potential-Energy Surfaces, *Physical Review Letters* **98**, 146401 (2007).
- [4] A. P. Bartók, M. C. Payne, R. Kondor, and G. Csányi, Gaussian Approximation Potentials: The Accuracy of Quantum Mechanics, without the Electrons, *Physical Review Letters* **104**, 136403 (2010).
- [5] S. Chmiela, A. Tkatchenko, H. E. Sauceda, I. Poltavsky, K. T. Schütt, and K.-R. Müller, Machine learning of accurate energy-conserving molecular force fields, *Science Advances* **3**, e1603015 (2017).
- [6] S. Chmiela, H. E. Sauceda, K.-R. Müller, and A. Tkatchenko, Towards exact molecular dynamics simulations with machine-learned force fields, *Nature Communications* **9**, 3887 (2018).
- [7] L. Zhang, J. Han, H. Wang, R. Car, and W. E, Deep Potential Molecular Dynamics: A Scalable Model with the Accuracy of Quantum Mechanics, *Physical Review Letters* **120**, 143001 (2018).
- [8] A. Seko, A. Takahashi, and I. Tanaka, First-principles interatomic potentials for ten elemental metals via compressed sensing, *Physical Review B* **92**, 054113 (2015).
- [9] K. T. Schütt, M. Gastegger, A. Tkatchenko, K. R. Müller, and R. J. Maurer, Unifying machine learning and quantum chemistry – a deep neural network for molecular wavefunctions, *Nature Communications* **10**, 5024 (2019).
- [10] Z. Li, J. R. Kermode, and A. De Vita, Molecular Dynamics with On-the-Fly Machine Learning of Quantum-Mechanical Forces, *Physical Review Letters* **114**, 096405 (2015).
- [11] R. Jinnouchi, F. Karsai, and G. Kresse, On-the-fly machine learning force field generation: Application to melting points, *Physical Review B* **100**, 014105 (2019).
- [12] R. Jinnouchi, J. Lahnsteiner, F. Karsai, G. Kresse, and M. Bokdam, Phase Transitions of Hybrid Perovskites Simulated by Machine-Learning Force Fields Trained on the Fly with Bayesian Inference, *Physical Review Letters* **122**, 225701 (2019).
- [13] J. Vandermause, S. B. Torrisi, S. Batzner, Y. Xie, L. Sun, A. M. Kolpak, and B. Kozinsky, On-the-fly active learning of interpretable Bayesian force fields for atomistic rare events, *npj Computational Materials* **6**, 20 (2020).
- [14] N. Artrith and J. Behler, High-dimensional neural network potentials for metal surfaces: A prototype study for copper, *Physical Review B* **85**, 045439 (2012).
- [15] N. Bernstein, G. Csányi, and V. L. Deringer, De novo exploration and self-guided learning of potential-energy surfaces, *npj Computational Materials* **5**, 99 (2019).
- [16] C. E. Rasmussen and C. K. I. Williams, *Gaussian Processes for Machine Learning* (The MIT Press, 2005).
- [17] M. Titsias, Variational Learning of Inducing Variables in Sparse Gaussian Processes, in *Proceedings of the Twelfth International Conference on Artificial Intelligence and Statistics*, Proceedings of Machine Learning Research, Vol. 5, edited by D. van Dyk and M. Welling (PMLR, Hilton Clearwater Beach Resort, Clearwater Beach, Florida USA, 2009) pp. 567–574.
- [18] V. L. Deringer and G. Csányi, Machine learning based interatomic potential for amorphous carbon, *Physical Review B* **95**, 094203 (2017).
- [19] A. P. Bartók, R. Kondor, and G. Csányi, On representing chemical environments, *Physical Review B* **87**, 184115 (2013).
- [20] See Supplemental Material at [URL will be inserted by publisher] for inclusion of the forces data in SGPR, computational cost, adaptive sampling, training and testing, RDFs, and visualizations.
- [21] K. Miwa and H. Ohno, Molecular dynamics study on  $\beta$ -phase vanadium monohydride with machine learning potential, *Physical Review B* **94**, 184109 (2016).
- [22] L. Foster, A. Waagen, N. Aijaz, M. Hurley, A. Luis, J. Rinsky, M. J. Way MICHAELJWAY, P. Gazis, and A. Srivastava, *Journal of Machine Learning Research*, Tech. Rep. (2009).
- [23] G. N. G. N. Watson, *A treatise on the theory of Bessel functions* (Cambridge University Press, 1995) p. 804.
- [24] S. De, A. P. Bartók, G. Csányi, and M. Ceriotti, Comparing molecules and solids across structural and alchemical space, *Physical Chemistry Chemical Physics* **18**, 13754 (2016).
- [25] G. Kresse and J. Furthmüller, Efficient iterative schemes for ab initio total-energy calculations using a plane-wave basis set, *Physical Review B - Condensed Matter and Materials Physics* **54**, 11169 (1996).
- [26] P. E. Blöchl, Projector augmented-wave method, *Physi-*

- cal Review B **50**, 17953 (1994).
- [27] J. P. Perdew, M. Ernzerhof, and K. Burke, Rationale for mixing exact exchange with density functional approximations, *Journal of Chemical Physics* **105**, 9982 (1996).
- [28] A. Hajibabaei, A python package for sparse Gaussian process regression of the ab-initio potential energy surface, <https://github.com/amirhajibabaei/AutoForce> (2019).
- [29] A. Hjorth Larsen, J. JØrgen Mortensen, J. Blomqvist, I. E. Castelli, R. Christensen, M. Dulak, J. Friis, M. N. Groves, B. Hammer, C. Hargus, E. D. Hermes, P. C. Jennings, P. Bjerre Jensen, J. Kermode, J. R. Kitchin, E. Leonhard Kolsbjerg, J. Kubal, K. Kaasbjerg, S. Lysgaard, J. Bergmann Maronsson, T. Maxson, T. Olsen, L. Pastewka, A. Peterson, C. Rostgaard, J. SchiØtz, O. Schütt, M. Strange, K. S. Thygesen, T. Vegge, L. Vilhelmsen, M. Walter, Z. Zeng, and K. W. Jacobsen, *The atomic simulation environment - A Python library for working with atoms* (2017).
- [30] A. Togo and I. Tanaka, First principles phonon calculations in materials science, *Scripta Materialia* **108**, 10.1016/j.scriptamat.2015.07.021 (2015).
- [31] F. Mizuno, A. Hayashi, K. Tadanaga, and M. Tatsumisago, High lithium ion conducting glass-ceramics in the system Li<sub>2</sub>S–P<sub>2</sub>S<sub>5</sub>, *Solid State Ionics* **177**, 2721 (2006).
- [32] H. Yamane, M. Shibata, Y. Shimane, T. Junke, Y. Seino, S. Adams, K. Minami, A. Hayashi, and M. Tatsumisago, Crystal structure of a superionic conductor, Li<sub>7</sub>P<sub>3</sub>S<sub>11</sub>, *Solid State Ionics* **178**, 1163 (2007).
- [33] I. H. Chu, H. Nguyen, S. Hy, Y. C. Lin, Z. Wang, Z. Xu, Z. Deng, Y. S. Meng, and S. P. Ong, Insights into the Performance Limits of the Li<sub>7</sub>P<sub>3</sub>S<sub>11</sub> Superionic Conductor: A Combined First-Principles and Experimental Study, *ACS Applied Materials and Interfaces* **8**, 7843 (2016).
- [34] Y. Wang, W. D. Richards, S. H. Bo, L. J. Miara, and G. Ceder, Computational Prediction and Evaluation of Solid-State Sodium Superionic Conductors Na<sub>7</sub>P<sub>3</sub>X<sub>11</sub> (X = O, S, Se), *Chemistry of Materials* **29**, 7475 (2017).
- [35] Y. Seino, T. Ota, K. Takada, A. Hayashi, and M. Tatsumisago, A sulphide lithium super ion conductor is superior to liquid ion conductors for use in rechargeable batteries, *Energy Environ. Sci.* **7**, 627 (2014).
- [36] Y. Seino, M. Nakagawa, M. Senga, H. Higuchi, K. Takada, and T. Sasaki, Analysis of the structure and degree of crystallisation of 70Li<sub>2</sub>S-30P<sub>2</sub>S<sub>5</sub> glass ceramic, *Journal of Materials Chemistry A* **3**, 2756 (2015).
- [37] D. Wohlmuth, V. Epp, and M. Wilkening, Fast Li Ion Dynamics in the Solid Electrolyte Li<sub>7</sub>P<sub>3</sub>S<sub>11</sub> as Probed by <sup>6,7</sup>Li NMR Spin-Lattice Relaxation, *ChemPhysChem* **16**, 2582 (2015).



**Supplemental Material for**  
**“Towards Universal Sparse Gaussian Process Potentials:**  
**Application to Lithium Diffusivity in Superionic Conducting Solid**  
**Electrolytes”**

Amir Hajibabaei, Chang Woo Myung, and Kwang S. Kim\*

(Dated: May 21, 2021)

**INCLUDING THE FORCES DATA**

Let  $x = \{\rho_i\}_{i=1}^N$  be the list of LCEs for a given configuration  $x$  and  $z = \{\chi_j\}_{j=1}^m$  the list of inducing LCEs for SGPR. The potential energy and forces obtained from FP calculations are  $E, f_i^\mu$  where  $i$  indexes the atoms and  $\mu$  the Cartesian dimensions. We define

$$\beta(x, z) = \sum_{i=1}^N \left[ \mathcal{K}(\rho_i, \chi_1), \dots, \mathcal{K}(\rho_i, \chi_m) \right]. \quad (\text{S1})$$

Then the covariance and data matrices for  $x$  become

$$k_{xm} = \begin{bmatrix} \beta(x, z) \\ \vdots \\ -\frac{\partial \beta(x, z)}{\partial r_i^\mu} \\ \vdots \end{bmatrix}, Y_x = \begin{bmatrix} E \\ \vdots \\ f_i^\mu \\ \vdots \end{bmatrix} \quad (\text{S2})$$

respectively, where  $r_i^\mu$  are the coordinates of atoms. These matrices are calculated for all configurations and are concatenated to build  $k_{nm}$  and  $Y$  defined in the main text.

**THE COST OF KERNEL FOR GPR AND SGPR**

For two configurations  $A = \{a_i\}_{i=1}^{N_A}$  and  $B = \{b_i\}_{i=1}^{N_B}$  where  $a_i, b_i$  are the per-atom descriptors, covariance of total energies is calculated by

$$\langle E_A E_B \rangle = \sum_{i, i'} \mathcal{K}(a_i, b_{i'}) \rightarrow c \propto N_A N_B, \quad (\text{S3})$$

where  $c$  is the computational cost. Let the average number of atoms in the neighborhood of each atom, within a cutoff radius  $r_c$ , be  $n_c$ . Covariance of a total energy and a force component is

---

\* kimks@unist.ac.kr

calculated by

$$\langle E_A F_{j'}^{\mu,B} \rangle = - \sum_{i,i'} \frac{\partial \mathcal{K}(a_i, b_{i'})}{\partial r_{j'}^{\mu}} \rightarrow c \propto N_A n_c, \quad (\text{S4})$$

since the index  $i'$  should cover all the atoms in the neighborhood of  $j'$ . Similarly, covariance of two force components is calculated by

$$\langle F_j^{\nu,A} F_{j'}^{\mu,B} \rangle = \sum_{i,i'} \frac{\partial^2 \mathcal{K}(a_i, b_{i'})}{\partial r_j^{\nu} \partial r_{j'}^{\mu}} \rightarrow c \propto n_c^2, \quad (\text{S5})$$

The total cost for the evaluation of kernel between two configurations, considering that there are  $3N_A$  and  $3N_B$  force components, becomes

$$\begin{aligned} c &\propto N_A N_B + (N_A n_c) \times (3N_B) + (N_B n_c) \times (3N_A) + n_c^2 (3N_A)(3N_B) \\ &\propto (1 + 3n_c)^2 N_A N_B \end{aligned} \quad (\text{S6})$$

In these equations the cost related to the length of the descriptor vector is factored.

**GPR:** In GPR we need to construct the full covariance matrix for the data given by  $X = \{x_i\}_{i=1}^n$ . The cost becomes

$$c_1 \propto \sum_{i,j=1}^n (1 + 3n_c)^2 N_i N_j \quad (\text{S7})$$

If all of the configurations in the data have the same number of atoms  $N$ , the cost of constructing the full covariance matrix is proportional to

$$c_1 \propto (1 + 3n_c)^2 N^2 n^2 \quad (\text{S8})$$

**SGPR:** In SGPR, we only need to calculate the kernel between all of the configurations and a set of inducing local chemical environments (LCEs)  $z = \{\rho_i\}_{i=1}^m$  as well as between LCEs themselves. The cost is

$$c_2 \propto (1 + 3n_c) N n m + m^2 \quad (\text{S9})$$

**Comparison:** If we ignore  $m^2$  in  $c_2$

$$\frac{c_2}{c_1} \propto \frac{m}{(1 + 3n_c) N n} \quad (\text{S10})$$

For a typical choice of sizes  $n = 100$ ,  $N = 100$ ,  $n_c = 33$ , and  $m = 1000$ , which occur in our simulations, the cost ratio becomes

$$\frac{c_2}{c_1} = \frac{1}{1000} \quad (\text{S11})$$

## ADAPTIVE SAMPLING ALGORITHM

For adaptive sampling of the data  $X$  and inducing LCEs  $z$ , the model is built on-the-fly with MD where the system  $x(t) = \{\chi_j(t)\}_{j=1}^N$  evolves with the SGPR potential, and FP calculations are carried out actively to correct the model based on the following criterion. The data and unique LCEs in the first step are automatically included in  $X$  and  $z$ . In the following steps, we try to insert on-the-fly LCEs to  $z$ . A LCE  $\chi_j$  is added to  $z$  only if  $\Delta E(\chi_j) > \epsilon$  where  $\Delta E$  is the change in the predictive energy resulting from inclusion of  $\chi_j$  in  $z$  and  $\epsilon$  is a predetermined threshold. Since it is too costly to try out all LCEs, in the spirit of importance sampling, we try insertion of LCEs based on their spilling factor (see main text) in a descending order and terminate at the first unsuccessful insertion trial. If at least one LCE is added to  $z$ , it means that the system has potentially crossed into an unfamiliar region. At this stage, in one algorithm (FAST), we calculated the exact FP energy and forces and included the snapshot  $x(t)$  in  $X$  only if  $\Delta E(x(t)) > \epsilon$ . Thus, sometimes the exact FP data were regarded as redundant and were rejected by the model. This was devised to keep the number of sampled data ( $\propto$  the computation cost in future steps) as small as possible. In another algorithm (ULTRAFast), in order to preempt unwanted FP calculations, predictions of the model were used as fake FP data and if the insertion was accepted they were corrected by exact calculations. This algorithm is similar to leave-one-out cross-validation method for active learning [1]. For promoting global exploration and speeding up the sampling, we only sample at the extrema of the on-the-fly potential energy (see Fig. S1). Special care must be taken for stabilizing the model in early steps.

## TRAINING AND TESTING

For true forces  $\{f_i\}$  and the model's predictions  $\{\tilde{f}_i\}$ , coefficient of determination (CD) of the model is defined by

$$R^2 = 1 - \frac{\sum_i (f_i - \tilde{f}_i)^2}{\sum_i (f_i - \bar{f})^2}. \quad (\text{S12})$$

Since CD is normalized by the variance in the data, it is a more consistent measure than root mean squared error (RMSE). For energies, it is more appropriate to use mean absolute error (MAE) because, unlike forces, energies are not distributed around zero and uniform shift does not affect RMSE.

As the first example in the main text, a SGPR potential is trained on-the-fly with MD, with three different systems:  $\gamma$ -Li<sub>3</sub>PS<sub>4</sub> with (1 × 1 × 2),  $\beta$ -Li<sub>3</sub>PS<sub>4</sub> with (2 × 1 × 1), and Li<sub>7</sub>P<sub>3</sub>S<sub>11</sub> with (2 × 1 × 1) cells. For sampling, the systems were quenched from ~1500 K to 700 K in ~5 ps by velocity re-scaling and kept at this temperature for ~45 ps using a time step of 2 fs. In quenching, there is no time for the crystal to melt (since atoms do not have time to displace too far the crystal becomes only locally disordered) but this local distortion results in stream of diverse LCEs to the sampling algorithm which helps in faster stabilization of the model at the beginning of training. This practice is beneficial but not compulsory. The algorithm FAST (see adaptive

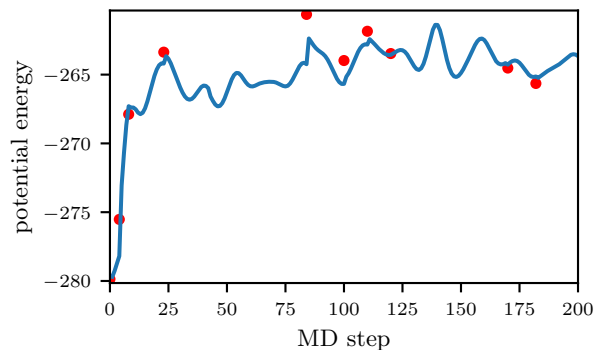


FIG. S1. On-the-fly predicted potential energy of the SGPR model at the beginning of MD. Red bullets indicate the timings and energies of FP calculations.

sampling algorithms in the main text) is applied in training (see Fig. S1), therefore in total only 456 FP calculations are performed from which only 111 are sampled by the model (as data  $X, Y$ ) and 705 LCEs are sampled as the inducing set ( $z$ ). For the sake of speed, only  $\Gamma$  point is selected for sampling  $k$ -space, but afterwards the potential energy and forces are recalculated with a  $2 \times 2 \times 2$   $k$ -point grid only for those 111 data which are included in the model. This corrects the forces by an RMSE of about  $0.04 \text{ eV \AA}^{-1}$ . In Fig. S2 performance of the model on all 456 examples is demonstrated.

To verify the model with independent data, MLMD simulations at five temperatures in the range 300 to 700 K for 0.8 to 2.2 ns are performed (only for  $\text{Li}_7\text{P}_3\text{S}_{11}$ , same size as training) and  $10^3$  snapshots are randomly selected. Accuracy of the model is tested with these samples in Fig. S3.

In addition, the liquid and glass phase  $\text{Li}_7\text{P}_3\text{S}_{11}$  are simulated with the SGPR model. Testing of the model in these phases is shown in Fig. S4. Since size of the cells in these simulations (672 atoms) are larger than the training systems, the SGPR model slightly underestimates the total energy (by  $\sim 3 \times 10^{-3} \text{ eV per-atom}$ ) due to the long-range forces that are excluded because of a finite cutoff radius. Treatment of the long-range forces with ML models is not trivial yet.

To demonstrate that the generated SGPR model is energy-conservative, an MD simulation in NVE ensemble is carried out which is shown in Fig. S5. A nudged elastic band (NEB) calculations is also carried out which is directly compared with DFT in Fig. S6.

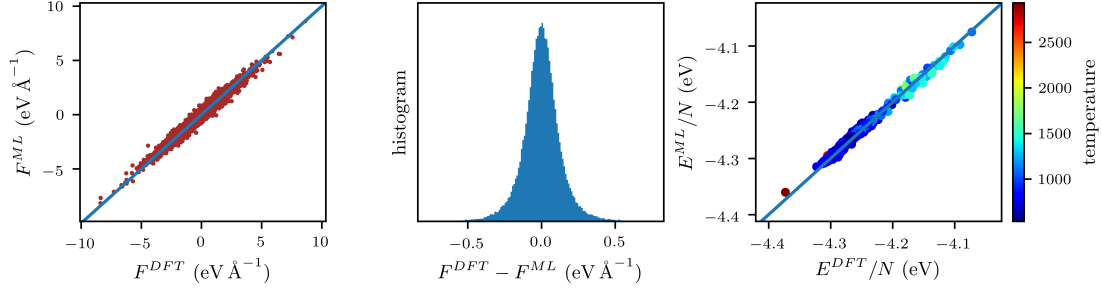


FIG. S2. **Training data:** testing the model trained with  $\text{Li}_3\text{PS}_4$  ( $\alpha$  and  $\beta$ ) and  $\text{Li}_7\text{P}_3\text{S}_{11}$  on all 456 FP calculations which were performed during training. For forces RMSE is  $0.13 \text{ eV \AA}^{-1}$  and  $R^2 = 0.967$ . For energies MAE is  $3.817 \times 10^{-3} \text{ eV}$  per-atom.

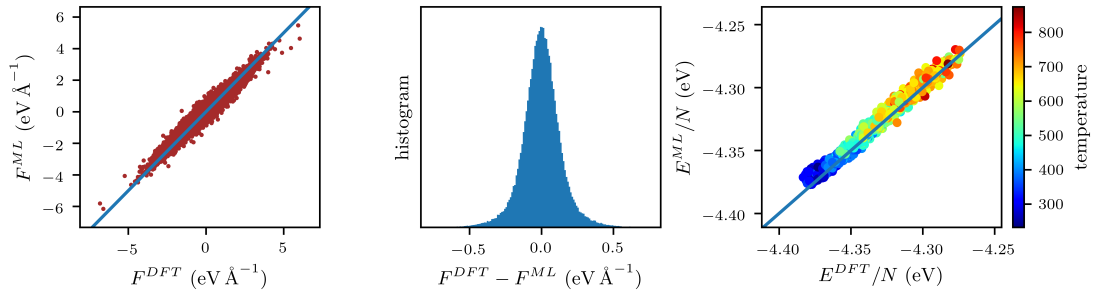


FIG. S3. **Crystal phase:** 1000 samples are randomly selected from extensive MLMD simulations of  $\text{Li}_7\text{P}_3\text{S}_{11}$  at five temperatures in the range 300 to 700 K for 0.8 to 2.2 ns. The number of atoms in these samples is 84. For forces RMSE is  $0.139 \text{ eV \AA}^{-1}$  and  $R^2 = 0.944$ . For energies MAE is  $3.822 \times 10^{-3} \text{ eV}$  per-atom.

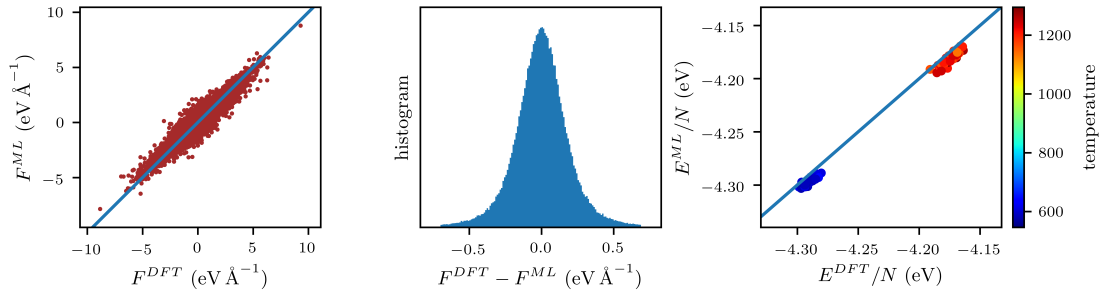


FIG. S4. **Liquid and glass phases:** 50+70 samples are drawn from MLMD simulation of the liquid phase  $\text{Li}_7\text{P}_3\text{S}_{11}$  at 1200 K and glass phase (obtained after melt-quenching) at 600 K for  $\sim 0.2$  ns. The number of atoms in these samples is 672. The errors in these phases are similar. For forces RMSE is  $0.21 \text{ eV \AA}^{-1}$  and  $R^2 = 0.917$ . For energies MAE is  $6.35 \times 10^{-3} \text{ eV}$  per-atom.

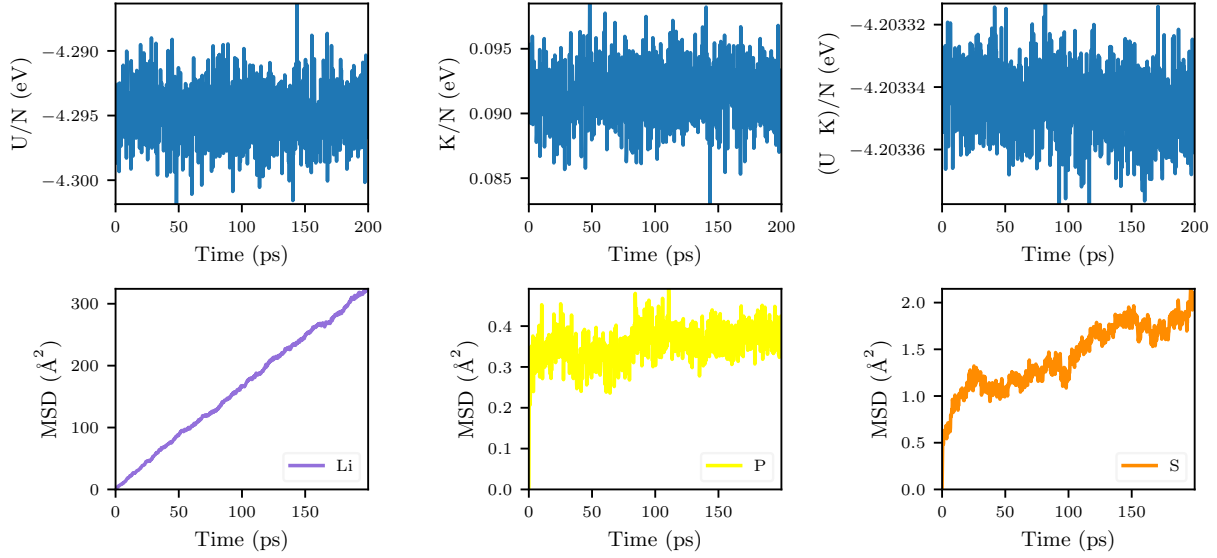


FIG. S5. **Energy conservation:** MLMD simulation of  $\text{Li}_7\text{P}_3\text{S}_{11}$  with 672 atoms in NVE ensemble with velocity-Verlet algorithm. The temperature is  $\sim 700$  K. The per-atoms potential energy, kinetic energy, and total energy are plotted in the first row. The total energy is conserved up to small fluctuations of  $\sim 10^{-5}$  eV per atom which are related to the finite timestep of 2 fs. In the second row, MSDs of atoms from their initial positions are plotted.

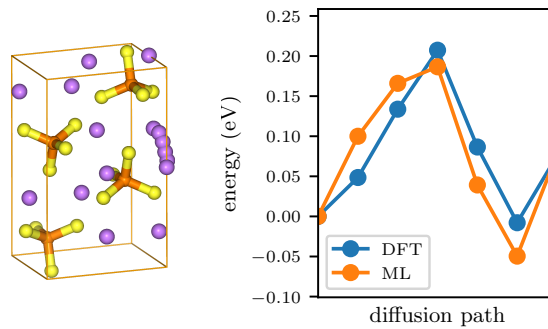


FIG. S6. Nudged elastic band calculations for Li hopping to a neighboring vacancy (created by Li removal) in  $\gamma\text{-Li}_3\text{PS}_4$  with DFT and ML potentials.  $(2 \times 2 \times 2)$  k-point grid is applied in DFT calculations.

## LARGE SCALE MLMD SIMULATIONS

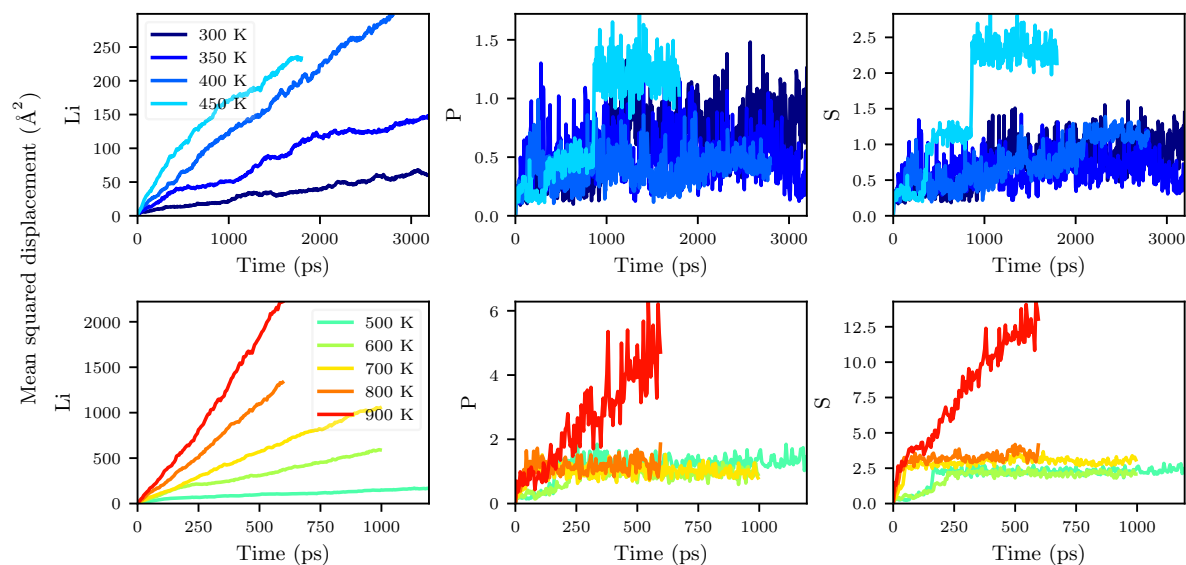


FIG. S7. Mean squared displacements of atoms in  $\text{Li}_7\text{P}_3\text{S}_{11}$  system (with 672 atoms) during the MD simulation in the NPT ensemble with temperatures ranging from 300 to 900 K. The jumps in the MSD of P and S atoms are associated with a crystal-crystal ( $\alpha \rightarrow \beta$ ) phase transition. The crystal melts at 900 K.

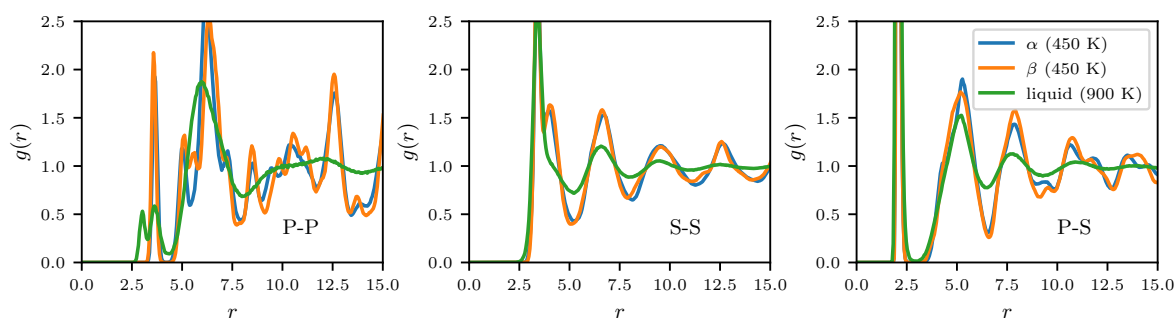


FIG. S8. Radial distribution functions in  $\alpha$ ,  $\beta$ , and molten phases of  $\text{Li}_7\text{P}_3\text{S}_{11}$ .

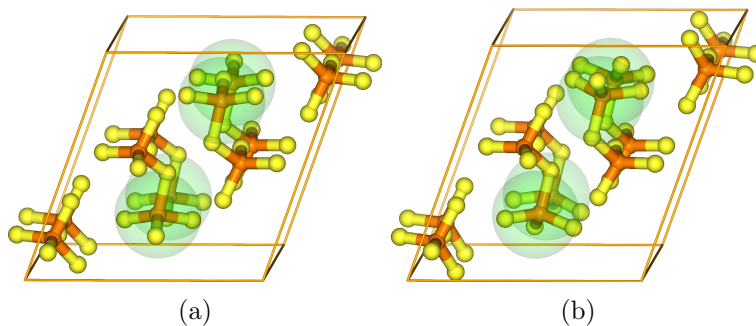


FIG. S9. Relaxed (a)  $\alpha$  and (b)  $\beta$  cells of  $\text{Li}_7\text{P}_3\text{S}_{11}$ , while Li atoms are removed for clarity. The rotated  $\text{PS}_4$  tetrahedra are highlighted with green.

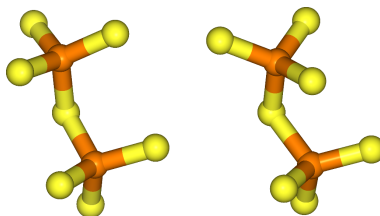


FIG. S10. Preferred orientations of  $\text{P}_2\text{S}_7$  double-tetrahedra in  $\alpha$  (left) and  $\beta$  (right) phases of  $\text{Li}_7\text{P}_3\text{S}_{11}$ .

## COMPUTATIONAL PERFORMANCE

For a system with  $N$  atoms, the computational cost of predicting energy and forces with the SGPR model is  $\mathcal{O}(N)$ , while the complexity of FP calculations is  $\mathcal{O}(N^3)$  or at best  $\mathcal{O}(N^2 \log N)$ . The elapsed time for FP calculations of the energy and forces for a system with 672 atoms was 9718s using VASP with 80 cores, while the elapsed time for the same calculation with SGPR was 5.3s using only 20 cores. The cost defined by elapsed  $\times$  cores/ $N$  is  $\sim 0.15$ s for SGPR which is better than FP calculations by a factor of  $\mathcal{O}(10^4)$ .

- 
- [1] H. Liu, Y. S. Ong, and J. Cai, A survey of adaptive sampling for global metamodeling in support of simulation-based complex engineering design (2018).
- [2] A. Jain, S. P. Ong, G. Hautier, W. Chen, W. D. Richards, S. Dacek, S. Cholia, D. Gunter, D. Skinner, G. Ceder, and K. A. Persson, Commentary: The materials project: A materials genome approach to accelerating materials innovation (2013).